




Cite this: *Mater. Adv.*, 2022, **3**, 3536

# Self-standing porous carbon electrodes for lithium–oxygen batteries under lean electrolyte and high areal capacity conditions†

Jittraporn Saengkaew,<sup>a</sup> Takashi Kameda,<sup>a</sup> Manai Ono<sup>a</sup> and Shoichi Matsuda<sup>ab</sup> 

The theoretical energy densities of lithium–oxygen batteries (LOBs) surpass those of lithium-ion batteries (LiBs). However, most of the LOBs reported contain excess electrolyte amounts and operate under low areal capacity conditions thereby exhibiting a cell-level energy density much lower than that of the LiBs. In the present study, we prepared a series of carbon powder-based self-standing membranes with different pore structures and investigated their battery performance under low electrolyte/areal capacity ( $E/C < 10 \text{ g A}^{-1} \text{ h}^{-1}$ ) conditions. Although, a clear correlation was observed between the total discharge capacity and pore volume of the carbon electrodes, the cycle number of the LOBs did not simply correlate with the total discharge capacity of the carbon electrodes. In particular, the carbon electrode mainly composed of mesopores exhibited superior cycle performance under low  $E/C$  conditions ( $E/C < 5 \text{ g A}^{-1} \text{ h}^{-1}$ ). We believe that the results obtained in this study show a new direction for the material design of porous carbon electrodes to realize LOBs with practically high energy density and long cycle life.

Received 29th October 2021,  
Accepted 1st March 2022

DOI: 10.1039/d1ma01001h

rsc.li/materials-advances

## Introduction

Rechargeable lithium–oxygen batteries (LOBs) have attracted much attention because of their high theoretical energy density, which surpasses that of the lithium-ion batteries (LiBs) (approximately  $300 \text{ W h kg}^{-1}$ ).<sup>1–5</sup> However, a majority of the related studies utilize large electrolyte excesses and operate under small areal capacity conditions. Therefore, most of the LOBs reported exhibited energy densities much lower than those of the LiBs, except for a few studies.<sup>6</sup> A recent study revealed that the ratio of electrolyte weight to cell capacity ( $E/C$ ,  $\text{g A}^{-1} \text{ h}^{-1}$ ), used as an empirical parameter of the electrolyte amount in the LiB, well describes the energy density of the LOBs.<sup>7–10</sup> Therefore, the materials should be evaluated under low  $E/C$  conditions ( $< 10 \text{ g A}^{-1} \text{ h}^{-1}$ ) to accurately predict the performance of the LOBs with a practically high energy density.

A typical LOB comprises a lithium metal foil, separator, lithium-ion-conducting organic electrolyte, porous carbon electrode, and gas-diffusion layer. During discharge, the lithium metal dissolves at the negative electrode. The generated electrons are

transferred to the positive electrode through an external circuit and used to reduce the atmospheric oxygen. In contrast, the lithium ions generated at the negative electrode are transported to the positive electrode through the electrolyte and form insoluble lithium peroxide ( $\text{Li}_2\text{O}_2$ ) as the discharge product.<sup>11,12</sup> The reversible reaction should proceed during the charging process. Therefore, an improvement in the positive electrode performance is required to realize LOBs with a practically high energy density. In particular, the hierarchical pore structure of the carbon electrode should be appropriately designed. In the positive-electrode reaction, the  $\text{Li}_2\text{O}_2$  generated during the discharge process accumulates on the carbon electrode pores. Thus, a carbon-based positive electrode is essential to ensure sufficient pore capacity for storing the deposited  $\text{Li}_2\text{O}_2$ .<sup>13,14</sup> In addition, interconnected macropores should be formed for efficient oxygen reduction under relatively high current density conditions, enhancing oxygen transport through the carbon electrode.<sup>15–21</sup> Although many studies have demonstrated architectures of hierarchically porous carbon electrodes with high surface areas and pore volumes, the performance of the LOBs was evaluated under relatively high  $E/C$  conditions ( $E/C > 50 \text{ g A}^{-1} \text{ h}^{-1}$ ). Thus, the ideal design strategy for the carbon electrodes to realize LOBs with a practically high energy density and long cycle life remains unclear.

Based on this background, in the present study, we investigated the relationship between the physicochemical properties

<sup>a</sup> Center for Green Research on Energy and Environmental Materials, National Institute for Material Science, 1-1 Namiki, Tsukuba, Ibaraki 305-0044, Japan.  
E-mail: matsuda.shoichi@nims.go.jp

<sup>b</sup> NIMS-SoftBank Advanced Technologies Development Center, National Institute for Material Science, 1-1 Namiki, Tsukuba, Ibaraki 305-0044, Japan

† Electronic supplementary information (ESI) available. See DOI: 10.1039/d1ma01001h

and performance of the carbon electrodes under relatively small E/C conditions ( $< 10 \text{ g A}^{-1} \text{ h}^{-1}$ ). A series of carbon-powder-based self-standing membranes with different pore structures were prepared by applying a non-solvent-induced phase separation (NIPS) technique.<sup>22–24</sup> The electrolyte amount dependence of the performance of the LOBs was systematically investigated by controlling the electrolyte amount inside the porous carbon electrode, which is realized using the stamping method recently developed by our group.<sup>25</sup>

## Experimental

### Preparation of carbon powder-based self-standing carbon membrane

A series of carbon power samples, SuperP (CENERGY, SUPER C65), VulcanX (VXC; CABOT VXC72), Black pearl (BP; CABOT. Black pearls 2000), Ketjen black (KB; Lion Specialty Chemicals Co., Ltd, EC600J), and ordered mesoporous carbon CMK-3 (CMK; ACS Material), were utilized for preparing a self-standing carbon membrane. A mixture slurry was prepared using 75 wt% of carbon powder, 5 wt% of single walled carbon nanotubes (OCSiAl, TUBALL, average fiber diameter of 1.6 nm and average length of 5  $\mu\text{m}$ ), 5 wt% of carbon fibers (Nippon Polymer Sangyo Co., Ltd, CF-N, average fiber diameter of 6  $\mu\text{m}$  and average length of 3 mm), 15 wt% of PAN, and NMP as a solvent for uniform dispersion. The mixture slurry was formed into a sheet by molding to a uniform thickness by a wet film forming method using a doctor blade. After molding, the sample was immersed in methanol (poor solvent) and converted to a porous film by the non-solvent induced phase separation method. Furthermore, a volatile solvent was removed by drying the sample at 80 °C for 10 h; subsequently heat treatment was performed (infusibilization treatment) at 230 °C for 3 h in an atmosphere using a box-type furnace (Denken High Dental Co., Ltd). Carbonization was performed by increasing the temperature to 1050 °C at a rate of 10 °C  $\text{min}^{-1}$  and maintaining a temperature of 1050 °C for 3 h and then allowing the sample to cool to room temperature. In all cases, the flow rate of gas was set to 800  $\text{mL min}^{-1}$ .

### Characterization of carbon powder-based self-standing carbon membrane

Micro-/mesoporous structures of the samples were characterized by nitrogen adsorption (3 FLEX, Micromeritics Instrument Corp.). Macropore size distributions were measured by mercury porosimetry (AutoporeIV 9505, Shimadzu Co.). Field-emission SEM (FE-SEM, S-4800, Hitachi) and SEM-EDS-EBSD (JSM-7800F, JEOL), and X-ray diffraction (XRD; SmartLab, Rigaku) were used to characterize the discharge products. Prior to the SEM and XRD analyses, the positive electrodes were removed from the electrochemical cells after the discharging process, washed three times with acetonitrile, and dried under vacuum. During sample preparation, the samples were not exposed to an ambient atmosphere.

### Lithium–oxygen cell assembly and discharge performance test

A solution of 1 M lithium bis(trifluoromethanesulfonyl)imide (LiTFSI; Kishida Chemical Co., Ltd, purity  $> 99.9\%$ ) dissolved in tetraethylene glycol dimethyl ether (TEGDME; Kishida Chemical Co., Ltd., purity  $> 99\%$ ) was used as the electrolyte. The water content of the electrolyte was less than 30 ppm and was measured by Karl Fischer titration. The carbon electrode was dried at 100 °C under vacuum for 12 h. Coin-type lithium–oxygen cells were assembled in a dry room with a water content of less than 10 ppm, by sequential stacking of metallic lithium foil (diameter = 16 mm, thickness = 0.2 mm; Honjo Metal Co., Ltd.), a glass fiber-based separator (diameter = 18 mm, thickness = 0.27 mm; Whatman GF-A), a carbon electrode (diameter = 16 mm, thickness = 0.27 mm), and a gas diffusion layer (diameter = 16 mm, thickness = 0.19 mm; TGP-H-060, Toray, Japan). During assembly, 100  $\mu\text{L}$  of the electrolyte was added to the separator. Electrochemical experiments were conducted using a battery-test equipment (SD8, Hokuto Denoko Corp.).

### Lithium–oxygen cell assembly and discharge/charge performance test

A solution of 0.5 M lithium bis(trifluoromethanesulfonyl)imide (LiTFSI; Kishida Chemical Co., Ltd, purity  $> 99.9\%$ ), 0.5 M  $\text{LiNO}_3$  (Sigma-Aldrich, purity  $> 99.9\%$ ) and 0.2 M LiBr (Sigma-Aldrich, purity  $> 99.9\%$ ) dissolved in tetraethylene glycol dimethyl ether (TEGDME; Kishida Chemical Co., Ltd, purity  $> 99\%$ ) was used as the electrolyte.  $\text{LiNO}_3$  and LiBr were dried at 120 °C under vacuum before using. The carbon electrode was dried at 100 °C under vacuum for 12 h. Lithium–oxygen cells were assembled in a dry room with a water content of less than 10 ppm, by sequential stacking of a lithium–metal foil (20 mm square, thickness of 0.1 mm; Honjo Metal Co., Ltd), polyolefin-based separator (22 mm square, thickness of 0.02 mm), ceramic-based solid-state separator (LICGC, thickness of 0.18 mm; Ohara, Inc.), polyolefin-based separator (22 mm square, thickness of 0.02 mm), porous carbon electrode (20 mm square), and gas-diffusion layer (thickness of 110  $\mu\text{m}$ , TGP-H-030, Toray). A ceramic-based solid-state separator was utilized for the protection of the lithium–metal negative electrode. Electrolyte injection into the carbon electrode was performed by the vacuum impregnation method. During assembly, 2.5  $\mu\text{L cm}^{-2}$  of the electrolyte was added to the separator. A pressure of 100 kPa was applied to the cell by a spring coil. Electrochemical experiments were conducted using a battery-test equipment (TOSCAT, Toyo System Co., Ltd.). The limiting capacity and cutoff voltage were set to 4.0  $\text{mA h cm}^{-2}$ , 2.0 V/4.5 V. The current density during discharging and charging process was set to 0.4 and 0.2  $\text{mA cm}^{-2}$ .

### Electrolyte filling method into the carbon electrode

In the case of the stamping method, a PTFE membrane (Advantec Toyo Co., Ltd., 22 mm square) was used as the hydrophilic filter. The porous carbon electrode was sandwiched between two hydrophilic filters impregnated with a suitable electrolyte amount (*via* drop-casting), and the electrode was kept under vacuum for more than 3 min. In all three methods,



the amount of the impregnated electrolyte was obtained as the electrode mass change upon filling.

### On-line MS analysis

A high-resolution MS instrument (M-201GA, CANON ANELVA Corp.) was utilized for on-line MS analysis. An electrochemical flow cell having an inner cell volume of approximately 25 mL (diameter = 50 mm; depth = 15 mm) was specially designed using the same components as for the Li-O<sub>2</sub> cells described above. The gas evolution during charging was continuously monitored by providing a flow of He gas through the cell at a rate of 2 mL min<sup>-1</sup>.

## Results and discussion

In the present study, a series of porous carbon powder samples, SuperP, Vulcan XC (VXC), Black Pearl (BP), Ketjen black (KB), and ordered mesoporous carbon CMK-3 (CMK), were utilized. The self-standing membranes were prepared by mixing porous carbon powders, carbon fibers, carbon nanotubes (CNTs), and polymeric materials. Carbon fibers and CNTs contribute to improving the mechanical strength of the membrane. A slurry mixture was prepared using 75 wt% carbon powder, 5 wt% carbon fibers, 5 wt% CNT, and 15 wt% PAN. During the membrane formation process, we applied the NIPS method. During the NIPS process, interconnected hierarchically macro-scale pores were formed, which is advantageous for efficient oxygen- and Li-ion transport through the membrane.<sup>26–28</sup> The details of the membrane preparation process are described in the literature.<sup>23</sup> The prepared membranes were dried and heat-treated under suitable conditions and subsequently calcinated at 1,050 °C in an inert atmosphere.

The physical properties of the prepared self-standing carbon membranes were investigated. The thickness, mass loading, and porosity of the prepared self-standing carbon membranes are summarized in Table 1. The carbon loading in the carbon powder-based self-standing membranes is in the range of 5.0–6.0 mg cm<sup>-2</sup> (average 5.5 mg cm<sup>-2</sup>). The thicknesses of SuperP-, VXC-, BP-, KB-, and CMK-based membranes are 240, 220, 330, 350, and 310 μm, respectively. Scanning electron microscopy (SEM) images of the prepared membranes are presented in Fig. 1. For the CMK-membrane, several micro meter sized particles were uniformly distributed (Fig. 1e). Notably, a turbostratic morphology with a three-dimensional hexagonal array of the mesoporous structure,<sup>29,30</sup> was evident by TEM analysis (Fig. S1, ESI†). For other prepared carbon membranes,

several hundred particles were distributed in the membrane and no distinct morphological difference was observed. Notably, CNTs were uniformly dispersed and promoted the cross-linking between carbon particles, thereby improving the mechanical strength of the membrane. The photographic images of each self-standing carbon membranes are also shown in Fig. 1f and Fig. S2 (ESI†).

The specific surface areas of the prepared membranes were analyzed using the Brunauer-Emmett-Teller (BET) method from the N<sub>2</sub> adsorption/desorption experiments; the pore structure was evaluated using the Barrett-Joyner-Halenda method. The BET surface areas and pore volumes of the carbon membrane and carbon power are shown in Fig. 2 and Fig. S3 (ESI†). Among the investigated carbon membrane samples, the SuperP- and VXC-based membranes exhibited relatively smaller BET surface areas (< 50 m<sup>2</sup> g<sup>-1</sup>) and pore volumes (< 0.1 cm<sup>3</sup> g<sup>-1</sup>). In contrast, the BP-, KB-, and CMK-based membranes showed higher BET surface areas (> 300 m<sup>2</sup> g<sup>-1</sup>) and pore volumes (> 0.3 cm<sup>3</sup> g<sup>-1</sup>). In particular, for the pore distribution of the carbon membranes, the KB-based membrane had pores in a wide region from 1 nm to 100 nm, while the CMK-based membrane had pores in a limited region of 3 nm to 8 nm. In contrast, the BP-based membrane had pores smaller than 3 nm and a region larger than 8 nm. Thus, the difference in the pore structure of the carbon membranes reflects the difference in the pore structure of the powders.

The discharging properties of the Li-O<sub>2</sub> cells equipped with a series of carbon membranes as the positive electrode were investigated using a coin-type cell. A solution of 1 M lithium bis(trifluoromethylsulfonyl)imide (LiTFSI) in TEGDME was used as the electrolyte for this experiment. Experiments were performed under excess electrolyte conditions using glass fiber as a separator to evaluate the performance of the discharge properties of the carbon membrane series. Fig. 3a and b present the discharge profiles of the Li-O<sub>2</sub> cell that is assembled with carbon powder-based electrodes. All cells exhibited a discharge plateau above 2.6 V associated with the discharge reaction progress. As shown in Fig. 3b, the Li-O<sub>2</sub> cell with the KB-based membrane exhibited the highest specific capacity of 2658 mA h g<sub>electrode</sub><sup>-1</sup>. Discharge capacities of 1447 mA h g<sub>electrode</sub><sup>-1</sup> and 977 mA h g<sub>electrode</sub><sup>-1</sup> were observed in the BP- and CMK-based membranes, respectively. In contrast, the SuperP- and VXC-based membranes demonstrate low specific capacities of 796 mA h g<sub>electrode</sub><sup>-1</sup> and 735 mA h g<sub>electrode</sub><sup>-1</sup>, respectively, as shown in Fig. 3a. Fig. 3c and d illustrate the relationship between the discharge capacity and physicochemical properties of the carbon membranes (BET surface area and pore volumes). Both parameters showed a positive correlation with the discharge capacity. Thus, the pore volume affects the discharge capacity more than the BET surface area, as observed by comparing the results of BP- and KB-based membranes.

Repeated discharge/charge tests were conducted to evaluate the performance of the series of the carbon membranes as positive electrodes for LOBs. We utilized stacked configuration-type Li-O<sub>2</sub> cells (Fig. S4, ESI†) and redox mediator containing electrolyte (0.5 M LiTFSI + 0.5 M LiNO<sub>3</sub> + 0.2 M LiBr in TEGDME) for this experiment. A solid-state ceramic-based

**Table 1** Property of carbon powder-based self-standing membranes

| Sample | Mass loading (mg cm <sup>-2</sup> ) | Thickness (μm) | Porosity (%) | BET surface area (m <sup>2</sup> g <sup>-1</sup> ) | Pore volume (cm <sup>3</sup> g <sup>-1</sup> ) |
|--------|-------------------------------------|----------------|--------------|--|--|
| SuperP | 5.0                                 | 240            | 89           | 24.32  | 0.0350   |
| VXC    | 6.0                                 | 220            | 86           | 44.54  | 0.0833   |
| BP     | 5.3                                 | 330            | 89           | 638.82   | 0.5569   |
| KB     | 5.5                                 | 350            | 92           | 649.43   | 0.8744   |
| CMK    | 5.8                                 | 310            | 92           | 337.93   | 0.3844   |





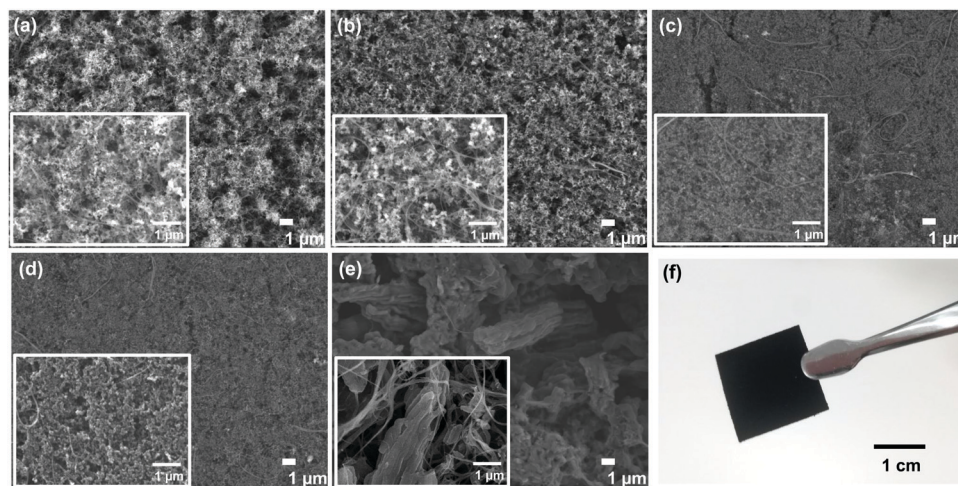


Fig. 1 SEM images of (a) SuperP-, (b) VXC-, (c) Black pearl-, (d) KB-, and (e) CMK-based self-standing membranes. Inset pictures present the higher magnified areas. (f) Photographic image of CMK-based self-standing membranes.

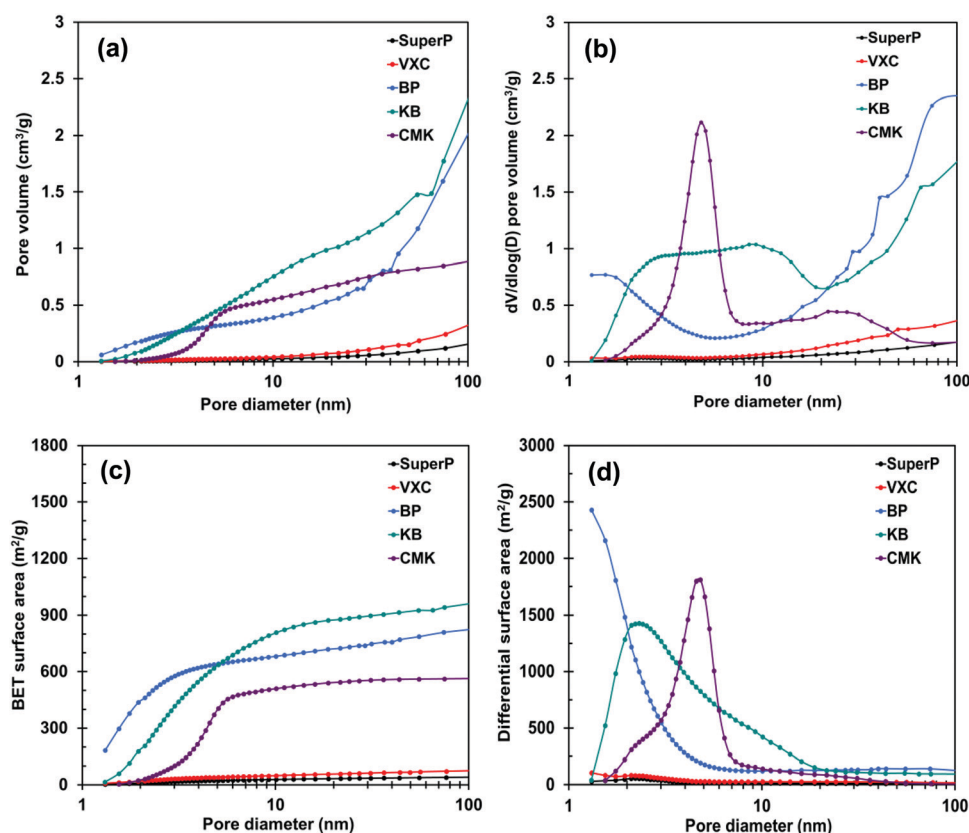


Fig. 2 Pore volume and BET surface area of series of self-standing carbon membranes.

separator was utilized for the repeated discharge/charge cycle test to minimize the side reaction of the Li metal negative electrode. Fig. 4a and b illustrate the first discharge/charge cycle of the Li-O<sub>2</sub> cells equipped with a series of carbon membranes as the positive electrode having a capacity limitation of 4 mA h cm<sup>-2</sup>. It should be noted that the cycle performance test with capacity limitation conditions is common

method for evaluate the performance of LOBs.<sup>2,31,32</sup> In this experiment, the electrolyte amount was quantitatively controlled to evaluate the performance of the Li-O<sub>2</sub> cells under low E/C conditions. The electrolyte amount at the positive electrode side and the E/C value of each cell are summarized in Table 2. During the discharge process, all the cells exhibited a voltage plateau at approximately 2.6 V. The voltage plateau was maintained up to



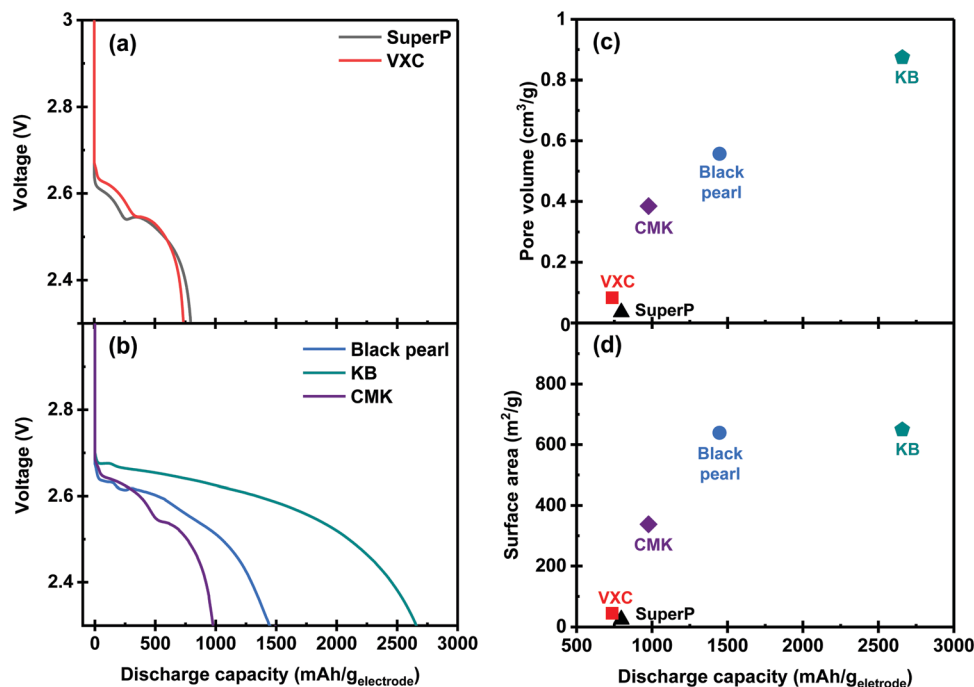


Fig. 3 (a and b) Discharge profile of lithium-oxygen cells with SuperP-, and VXC-, Black pearl-, KB- and CMK-based membranes as positive electrodes. (c and d) Relationships between discharge capacity, pore volume, and surface area of the carbon powder-based self-standing membranes.

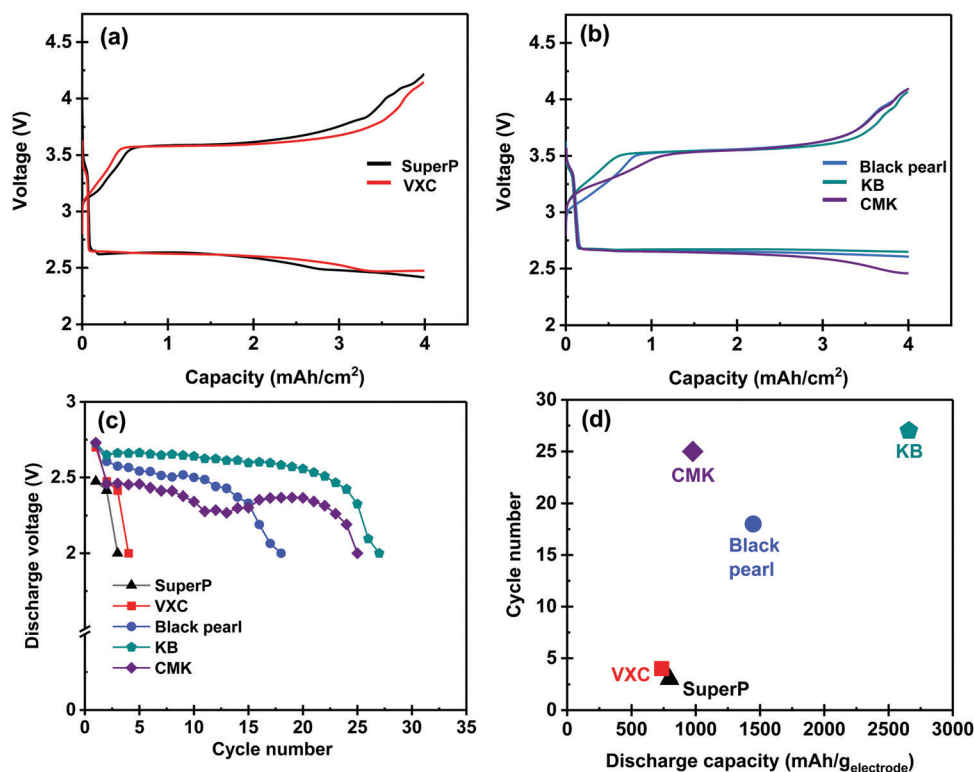


Fig. 4 (a and b) Discharge/charge profile and (c) cyclability of lithium-oxygen cells with SuperP-, and VXC-, Black pearl-, KB- and CMK-based membranes as positive electrodes. (d) Relationships between discharge capacity and cycle number for lithium-oxygen cells.

4 mA h cm<sup>-2</sup> for the cells equipped with BP- and KB-based electrodes. In contrast, a decrease in the voltage associated with

the progress of the discharge process was observed for the cells equipped with SuperP-, VXC-, and CMK-based electrodes, which



**Table 2** The electrolyte amount at the positive electrode side and the E/C value of each LAB cells

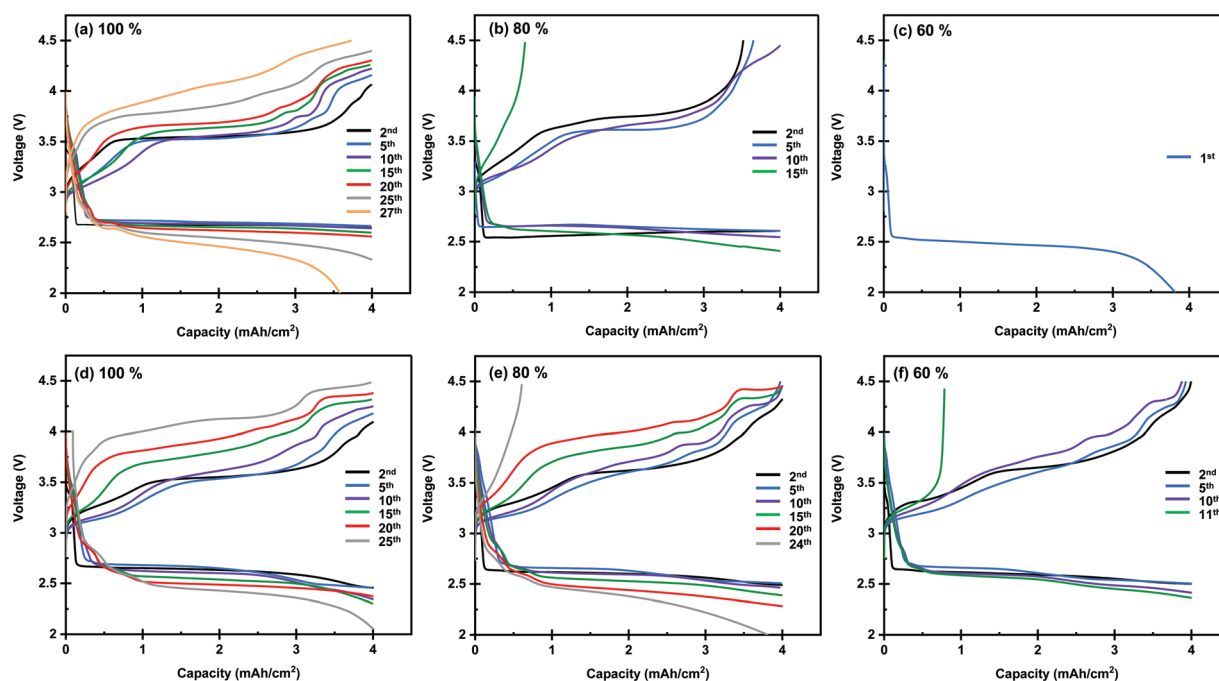
| Carbon electrode | Electrolyte injection ratio (%) | Carbon mass loading    | Electrolyte amount     |                                      | E/C |
|------------------|---------------------------------|------------------------|------------------------|--------------------------------------|-----|
|                  |                                 | (mg cm <sup>-2</sup> ) | (μL cm <sup>-2</sup> ) | (g A <sup>-1</sup> h <sup>-1</sup> ) |     |
| SuperP           | 100                             | 5.0                    | 22.1                   | 19.7                                 | 5.5 |
| VXC              | 100                             | 6.0                    | 21.2                   | 18.9                                 | 5.3 |
| BP               | 100                             | 5.3                    | 23.5                   | 21.0                                 | 5.9 |
| KB               | 100                             | 5.5                    | 25.8                   | 23.0                                 | 6.5 |
| KB               | 80                              | 5.5                    | 20.5                   | 18.3                                 | 5.1 |
| KB               | 60                              | 5.5                    | 15.2                   | 13.6                                 | 3.8 |
| CMK              | 100                             | 5.8                    | 28.3                   | 25.3                                 | 7.1 |
| CMK              | 80                              | 5.8                    | 22.6                   | 20.2                                 | 5.7 |
| CMK              | 60                              | 5.8                    | 17.0                   | 15.2                                 | 4.3 |

reached at approximately 2.5 V at the end of the discharging process. In the charging process, all the cells demonstrated a similar voltage profile, exhibiting a stable voltage plateau at approximately 3.5–3.6 V during the initial and middle part of the charging process. The voltage gradually increased to 4.2 V at the end of the charging process. The obtained results represent the charging profile of the Li–O<sub>2</sub> cell containing LiNO<sub>3</sub> and LiBr as the redox mediator.<sup>31–35</sup> The final discharge voltage value in each cell cycle was plotted against the cycle number (Fig. 4c). The cells equipped with SuperP- and VXC-based electrodes reached the cutoff condition at the 3rd and 4th cycles, respectively. In contrast, the cells equipped with BP-, CMK-, and KB-based electrodes exhibited higher cycle numbers up to the 18th, 25th, and 27th cycles, respectively. Although the cell with the CMK-based electrode exhibited a lower final discharge voltage than that of the KB-based electrode during the 1st–15th cycle, a stable cycle was maintained even over the 15th

cycle. The capacity value of each carbon electrode, obtained by the discharge performance test (Fig. 3a and b), was plotted against the cycle number of repeated discharge/charge tests (Fig. 4d). An evident correlation between the two factors was observed, except for the CMK-based electrode, suggesting that a higher capacity of the electrode was beneficial for achieving a prolonged cycle. In contrast, the CMK-based electrode showed a different tendency among the investigated samples.

We further investigated the Li–O<sub>2</sub> cells equipped with the KB- and CMK-based electrodes, which exhibited superior cycle performance. X-ray diffraction (XRD) analysis was performed for the KB- and CMK-based electrodes, which were removed from the Li–O<sub>2</sub> cells after the 1st discharging process with a capacity limitation of 2 mA cm<sup>-2</sup>. The peaks can be assigned to Li<sub>2</sub>O<sub>2</sub> (Fig. S5, ESI†), and the peak intensity is almost similar between the samples, suggesting that the Li<sub>2</sub>O<sub>2</sub> crystallinity is insignificantly different regardless of the carbon electrode type. In addition, the SEM analysis also revealed the uniform distribution of the crystalline compounds on both KB- and CMK-based electrodes after the discharging process (Fig. S6, ESI†).

The details of the charging process were also investigated by performing on-line mass spectrometry (MS) techniques.<sup>31,36,37</sup> The efficient oxygen evolution at the theoretical ratio of two-electron reduction reaction was observed as the charging proceeded in the Li–O<sub>2</sub> cells with a KB-based electrode (Fig. S7, ESI†), suggesting the advancement of the Li<sub>2</sub>O<sub>2</sub> decomposition. A gradual reduction in the oxygen evolution rate and the generation of H<sub>2</sub>O and CO<sub>2</sub> were observed, which were considered as the decomposition products of the TEGDME solvent.<sup>38</sup> Notably, an essentially similar on-line MS profile was obtained in the Li–O<sub>2</sub> cells with the CMK-based electrode

**Fig. 5** Discharge/charge profile of lithium–oxygen cells using (a–c) KB-, and (d–f) CMK-based membranes as the positive electrode with different electrolyte amount conditions.

(Fig. S7, ESI†). These results reveal that the charging reaction mechanism does not change significantly, depending on the structure of the carbon electrode.

Next, we investigated the performance of the Li-O<sub>2</sub> cells under lean electrolyte conditions. The above experiments were conducted under the condition in which the entire pore volume of the carbon electrode was fully wetted with the electrolyte. The amount of electrolyte injected into the carbon electrodes can be quantitatively controlled by the electrolyte injection technique, which was recently developed by our group.<sup>25</sup> Briefly, the use of two highly hydrophilic filters as electrolyte transfer agents allows the uniformly spread electrolyte to be transferred to the carbon electrode sandwiched between them. Fig. 5 presents the discharge/charge profiles of lithium-oxygen cells with electrolyte amounts of 100%, 80%, and 60% against the pore volume of the carbon electrode. As can be seen, the cell of the KB-based electrode exhibits a gradual increase in the overpotential, and the discharge/charge reaction suddenly drops in the 30th cycle. On the other hand, the cell of the CMK-based electrode operates slowly degraded charge and discharge terminal voltage, leading to increased gradual polarization, as shown in Fig. 5d. The improvement in the cell is noticeable when compared to the cycling profile of the lean electrolyte (80% and 60% of the electrolyte in the electrode). The KB-based electrode with 80% electrolyte maintained a high coulombic efficiency until the 10th cycle and failed in the 15th cycle. Additionally, in the lean electrolyte (60%) of the KB-based electrode, the charge voltage reached its cutoff voltage at the 2nd cycle. However, a gradual increase in the overpotential in both the discharging and charging profiles can be observed in a cell of a CMK-based electrode with 80% electrolyte. A lower cycling ability was observed for cells with a lower electrolyte amount (60%); thus, a stable discharge/charge profile was observed until the 10th cycle, and the charging profile of the cell reached the cutoff voltage at the 11th cycle. These results demonstrate that the CMK-based electrode can maintain a much lower overpotential of the discharge/charge profile even with lean electrolytes of 80% and 60% in the electrode. The performance of LOBs investigated in the present study and reported in the literature is summarized in Fig. 6 and Table S1

(ESI†) (ref. 23, 27 and 39–44). The LOBs equipped with CMK-based electrode prepared in the present study exhibited the one of the best performances, especially in the region of  $E/C < 5 \text{ g A}^{-1} \text{ h}^{-1}$ .

Herein, let us summarize the results obtained for the KB- and CMK-based electrodes. The XRD and online MS analyses results revealed no apparent differences between the two electrodes. In contrast, the cell degradation behavior and electrolyte amount dependency showed an evident difference. When the electrolyte injection ratio in the carbon electrode was 100%, the CMK-based electrode cell showed a gradual increase in overpotential during the cycle for both discharging and charging processes. In contrast, the increase in overpotential during cycles in the KB-based electrode cell was smaller than that of the CMK-based electrode. In the case of electrolyte injection ratios of 80% and 60%, the CMK-based electrode cell shows superior performance compared to the KB-based electrode cell. Such a difference in performance can be explained by the difference in the pore structures of the carbon electrodes. The KB-based electrode possesses a relatively high pore volume in the wide-scale regions (2–50 nm). Such a high pore volume and surface area result in a high capacity of the electrodes, contributing to the realization of prolonged discharge/charge cycles. Although the solid-state side products were formed during repeated cycles, the high pore volume and surface area could accommodate the deposited products without diminishing the battery performance. Consequently, the design strategy of the carbon electrodes for maximizing their pore volumes and surface areas is reasonably effective. However, such a strategy is not advantageous in limited electrolyte conditions because a high electrolyte amount is required to wet the surface of the electrodes fully. In particular, micropores with a size of 2 nm or less, which do not contribute to the discharge capacity, only increase the required electrolyte amount. Thus, the limited pore volume in the microporous region in the CMK-based electrode contributes to the superior performance under limited electrolyte conditions, although the capacity of the electrode is less than half that of the KB-based electrode.

## Conclusions

In the present study, we prepared five types of carbon powder-based self-standing membranes. Furthermore, we evaluated their performance as positive electrodes in LOBs with small  $E/C$  conditions, a requirement for realizing LOBs with a practically high energy density. Although the CMK-based electrode has less than half the capacity of the KB-based electrode, the cell equipped with the CMK-based electrode exhibited the best performance among the investigated samples. The KB-based electrode has a relatively large pore volume and high surface area, exhibiting the highest electrode capacity among the investigated samples. However, the high pore volume in microporous regions requires excess electrolyte amounts to wet the surface of the electrodes fully, diminishing their performance at relatively small conditions of the electrolyte injection ratio into the carbon electrodes.

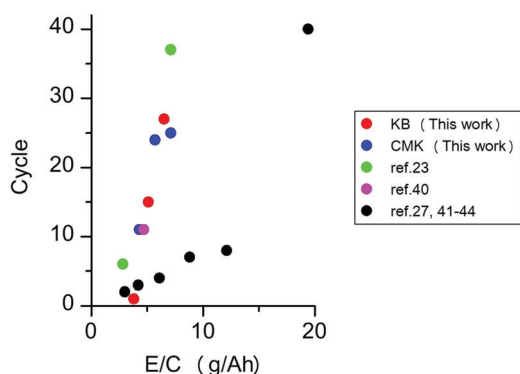


Fig. 6 Relationships between the cycle performance and the ratio of the electrolyte weight to cell capacity ( $E/C$ ,  $\text{g A}^{-1} \text{ h}^{-1}$ ).





In contrast, most of the pores selectively existed in the mesoporous region for the CMK-based electrode. Thus, the unique pore structure is beneficial for exhibiting superior LOB performance under small E/C conditions. We believe that the results obtained in the present study enlighten a new direction for the material design of porous carbon electrodes to realize LOBs with a practically high energy density and long cycle life.

## Author contributions

J. S., T. K., and S. M. conceived and designed the experiments. T. K. prepared the samples. J. S. and M. O. performed the analytical experiments. J. S., K. T., M. O., and S. M. discussed the results and analysed the data. J. S. and S. M. wrote the manuscript.

## Conflicts of interest

There are no conflicts to declare.

## Acknowledgements

The present work was partially supported by the ALCA-SPRING (Advanced Low Carbon Technology Research and Development Program – Specially Promoted Research for Innovative Next Generation Batteries) Project of the Japan Science and Technology Agency (JST: Grant Number JPMJAL1301). This work also received support from the National Institute for Materials Science (NIMS) Battery Research Platform.

## Notes and references

- 1 R. A. Wong, A. Dutta, C. Yang, K. Yamanaka, T. Ohta, A. Nakao, K. Waki and H. R. Byon, Structurally Tuning  $\text{Li}_2\text{O}_2$  by Controlling the Surface Properties of Carbon Electrodes: Implications for Li- $\text{O}_2$  Batteries, *Chem. Mater.*, 2016, **28**(21), 8006–8015.
- 2 A. Nomura, K. Ito and Y. Kubo, CNT Sheet Air Electrode for the Development of Ultra-High Cell Capacity in Lithium-Air Batteries, *Sci. Rep.*, 2017, **7**, 45596.
- 3 K.-N. Jung, J. Kim, Y. Yamauchi, M.-S. Park, J.-W. Lee and J. H. Kim, Rechargeable Lithium-Air Batteries: A Perspective on the Development of Oxygen Electrodes, *J. Mater. Chem. A*, 2016, **4**, 14050–14068.
- 4 W. Yang, Z. Qian, C. Du, C. Hua, P. Zuo, X. Cheng, Y. Ma and G. Yin, Hierarchical Ordered Macroporous/Ultrathin Mesoporous Carbon Architecture: A Promising Cathode Scaffold with Excellent Rate Performance for Rechargeable Li- $\text{O}_2$  Batteries, *Carbon*, 2017, **118**, 139–147.
- 5 G. Girishkumar, B. McCloskey, A. C. Luntz, S. Swanson and W. Wilcke, Lithium-Air Battery: Promise and Challenges, *J. Phys. Chem. Lett.*, 2010, **1**(14), 2193–2203.
- 6 J. O. Park, M. Kim, J.-H. Kim, K. H. Choi, H. C. Lee, W. Choi, S. B. Ma and D. Im, A 1000 W h  $\text{kg}^{-1}$  Li-Air Battery: Cell Design and Performance, *J. Power Sources*, 2019, **419**, 112–118.
- 7 M. Ue, K. Sakaushi and K. Uosaki, Basic Knowledge in Battery Research Bridging the Gap Between Academia and Industry, *Mater. Horiz.*, 2020, **7**, 1937–1954.
- 8 S. J. An, J. Li, C. Daniel, H. M. Meyer III, S. E. Trask, B. J. Polzin and D. L. Wood III, Electrolyte Volume Effects on Electrochemical Performance and Solid Electrolyte Interphase in Si-Graphite/NMC Lithium-Ion Pouch Cells, *ACS Appl. Mater. Interfaces*, 2017, **9**(22), 18799–18808.
- 9 S. J. An, J. Li, D. Mohanty, C. Daniel, B. J. Polzin, J. R. Croy, S. E. Trask and D. L. Wood III, Correlation of Electrolyte Volume and Electrochemical Performance in Lithium-Ion Pouch Cells with Graphite Anodes and NMC532 Cathodes, *J. Electrochem. Soc.*, 2017, **164**(6), A1195–A1202.
- 10 N. P. Lebedeva, F. D. Persio, T. Kosmidou, D. Dams, A. Pfrang, A. Kersys and L. Boon-Brett, Amount of Free Liquid Electrolyte in Commercial Large Format Prismatic Li-Ion Battery Cells, *J. Electrochem. Soc.*, 2019, **166**(4), A779–A786.
- 11 K. Sakai, S. Iwamura and S. R. Mukai, Influence of the Porous Structure of the Cathode on the Discharge Capacity of Lithium-Air Batteries, *J. Electrochem. Soc.*, 2017, **164**(13), A3075–A3080.
- 12 A. Bhargava and Y. Fu, Lithium Peroxide-Carbon Composite Cathode for Closed System Li- $\text{O}_2$  Batteries, *J. Electrochem. Soc.*, 2015, **162**(7), A1327–A1333.
- 13 C. Shen, J. Xie, T. Liu, M. Zhang, P. Andrei, L. Dong, M. Hendrickson, E. J. Plichta and J. P. Zheng, Influence of Pore Size on Discharge Capacity in Li-Air Batteries with Hierarchically Macroporous Carbon Nanotube Foams as Cathodes, *J. Electrochem. Soc.*, 2018, **165**(11), A2833–A2839.
- 14 Y. Zhang, H. Zhang, J. Li, M. Wang, H. Nie and F. Zhang, The Use of Mixed Carbon Materials with Improved Oxygen Transport in a Lithium-Air Battery, *J. Power Sources*, 2013, **240**, 390–396.
- 15 Y. Li, X. Li, D. Geng, Y. Tang, R. Li, J.-P. Dodelet, M. Lefèvre and X. Sun, Carbon Black Cathodes for Lithium Oxygen Batteries: Influence of Porosity and Heteroatom-Doping, *Carbon*, 2013, **64**, 170–177.
- 16 S.-M. Xu, X. Liang, Z.-C. Ren, K.-X. Wang and J.-S. Chen, Free-Standing Air Cathodes Based on 3D Hierarchically Porous Carbon Membranes: Kinetic Overpotential of Continuous Macropores in Li- $\text{O}_2$  Batteries, *Angew. Chem., Int. Ed.*, 2018, **57**, 6825–6829.
- 17 M. B. Osman, W. Yin, T. Petenzi, B. Josselme, R. Cornut, E. Raymundo-Pinero, A. Grimaud and C. L. Robert, Electrospun Carbon Fibers as Air Cathodes for Aprotic Li- $\text{O}_2$  Battery: Towards Cathode Design for Enhanced Capacity, *Electrochim. Acta*, 2020, **354**, 136643.
- 18 N. Kuanusont and Y. Shimoyama, Porous Carbon Cathode Assisted with Ionogel Binder Fabricated from Supercritical Fluid Technique toward Li- $\text{O}_2$ /CO $_2$  Battery Application, *ACS Appl. Energy Mater.*, 2020, **3**(5), 4421–4431.
- 19 M. Lee, Y. Yoo, J. H. Kwak, Y. S. Yun, H.-G. Jung, D. Byun, S. H. Oh and H.-D. Lim, Effect of Surface Characteristics of Carbon Host on Electrochemical Performance of Nonaqueous Li- $\text{O}_2$  Batteries, *Chem. Eng. J.*, 2021, **412**, 128549.





- 20 Y. Cao, H. Lu, B. Xu, W. Yang and Q. Hong, Nitrogen/Sulfur Dual-Doped Porous Carbon Nanofibers with  $\text{Co}_9\text{S}_8$  Nanoparticles Encapsulated by Graphitic Shells: A Highly Active Stable Free-Standing Air Electrode for Rechargeable Non-Aqueous  $\text{Li-O}_2$  Batteries and Primary Alkaline Al-Air Batteries, *Chem. Eng. J.*, 2019, **378**, 122247.
- 21 A. Dutta, R. A. Wong, W. Park, K. Yamanaka, T. Ohta, Y. Jung and H. R. Byon, Nanostructuring One-Dimensional and Amorphous Lithium Peroxide for High Round-Trip Efficiency in Lithium-Oxygen Batteries, *Nat. Commun.*, 2018, **9**(680), 1–10.
- 22 C. T.-C. Wan, R. R. Jacquemond, Y.-M. Chiang, K. Nijmeijer, F. R. Brushett and A. Forner-Cuenca, Non-Solvent Induced Phase Separation Enables Designer Redox Flow Battery Electrodes, *Adv. Mater.*, 2021, **33**, 2006716.
- 23 S. Matsuda, E. Yasukawa, T. Kameda, S. Kimura, S. Yamaguchi, Y. Kubo and K. Uosaki, Carbon-Black-Based Self-Standing Porous Electrode for 500 Wh/kg Rechargeable Lithium-Oxygen Batteries, *Cell Rep. Phys. Sci.*, 2021, **2**(7), 100506.
- 24 C.-Y. Tsai, K.-J. Peng, C.-F. Wang and Y.-L. Liu, Creation of Lithium-Ion-Conducting Channels in Gel Polymer Electrolytes through Non-Solvent-Induced Phase Separation for High-Rate Lithium-Ion Batteries, *ACS Sustainable Chem. Eng.*, 2020, **8**(5), 2138–2146.
- 25 S. Matsuda, S. Yamaguchi, E. Yasukawa, H. Asahina, H. Kakuta, H. Otani, S. Kimura, T. Kameda, Y. Takayanagi, A. Tajika, Y. Kubo and K. Uosaki, Effect of Electrolyte Filling Technology on the Performance of Porous Carbon Electrode-Based Lithium-Oxygen Batteries, *ACS Appl. Energy Mater.*, 2021, **4**(3), 2563–2569.
- 26 J. Fu, X. Guo, H. Huo, Y. Chen and T. Zhang, Easily Decomposed Discharge Products Induced by Cathode Construction for Highly Energy-Efficient Lithium-Oxygen Batteries, *ACS Appl. Mater. Interfaces*, 2019, **11**(16), 14803–14809.
- 27 W.-B. Luo, S.-L. Chou, J.-Z. Wang, Y.-C. Zhai and H.-K. Liu, A Metal-Free, Free-Standing, Macroporous Graphene@g- $\text{C}_3\text{N}_4$  Composite Air Electrode for High-Energy Lithium Oxygen Batteries, *Small*, 2015, **11**(23), 2817–2824.
- 28 H. Xue, S. Wu, J. Tang, H. Gong, P. He, J. He and H. Zhou, Hierarchical Porous Nickel Cobaltate Nanoneedle Arrays as Flexible Carbon-Protected Cathodes for High-Performance Lithium-Oxygen Batteries, *ACS Appl. Mater. Interfaces*, 2016, **8**(13), 8427–8435.
- 29 M. Kim, E. Yoo, W.-S. Ahn and S. E. Shim, Controlling Porosity of Porous Carbon Cathode for Lithium Oxygen Batteries: Influence of Micro and Meso Porosity, *J. Power Sources*, 2018, **389**, 20–27.
- 30 S. Fang, L. Shen, H. Zheng, Z. Tong, G. Pang and X. Zhang, Confined Germanium Nanoparticles in an N-Doped Carbon Matrix for High-Rate and Ultralong-Life Lithium Ion Batteries, *RSC Adv.*, 2015, **5**, 85256–85263.
- 31 X. Xin, K. Ito and Y. Kubo, Highly Efficient  $\text{Br}^-/\text{NO}_3^-$  Dual-Anion Electrolyte for Suppressing Charging Instabilities of  $\text{Li-O}_2$  Batteries, *ACS Appl. Mater. Interfaces*, 2017, **9**(31), 25976–25984.
- 32 W.-J. Kwak, D. Hirshberg, D. Sharon, M. Afri, A. A. Frimer, H.-G. Jung, D. Aurbach and Y.-K. Sun,  $\text{Li-O}_2$  Cells with  $\text{LiBr}$  as an Electrolyte and a Redox Mediator, *Energy Environ. Sci.*, 2016, **9**, 2334–2345.
- 33 S. Matsuda, S. Mori, K. Hashimoto and S. Nakanishi, Transition Metal Complexes with Macrocyclic Ligands Serve as Efficient Electrocatalysts for Aprotic Oxygen Evolution on  $\text{Li}_2\text{O}_2$ , *J. Phys. Chem. C*, 2014, **118**(49), 28435–28439.
- 34 J. Liu, T. Wu, S. Zhang, D. Li, Y. Wang, H. Xie, J. Yang and G. Sun,  $\text{InBr}_3$  as a Self-Defensed Redox Mediator for  $\text{Li-O}_2$  Batteries: In Situ Construction of a Stable Indium-Rich Composite Protective Layer on the Li Anode, *J. Power Sources*, 2019, **439**, 227095.
- 35 N. Togasaki, T. Gobara, T. Momma, T. Osaka and T. Numata, A Comparative Study of  $\text{LiNO}_3$  and  $\text{LiTFSI}$  for the Cycling Performance of  $\delta\text{-MnO}_2$  Cathode in Lithium-Oxygen Batteries, *J. Electrochem. Soc.*, 2017, **164**, A2225.
- 36 A. Dutta, K. Itoa and Y. Kubo, Nanoconfined Growth of Lithium-Peroxide inside Electrode Pores: A Noncatalytic Strategy toward Mitigating Capacity-Rechargeability Trade-Off in Lithium-Air Batteries, *Mater. Adv.*, 2021, **2**, 1302–1312.
- 37 W. Xu, V. V. Viswanathan, D. Wang, S. A. Towne, J. Xiao, Z. Nie, D. Hu and J.-G. Zhang, Investigation on the Charging Process of  $\text{Li}_2\text{O}_2$ -Based Air Electrodes in  $\text{Li-O}_2$  Batteries with Organic Carbonate Electrolytes, *J. Power Sources*, 2011, **196**(8), 3894–3899.
- 38 M. M. O. Thotiyil, S. A. Freunberger, Z. Peng, Y. Chen, Z. Liu and P. G. Bruce, A Stable Cathode for the Aprotic  $\text{Li-O}_2$  Battery, *Nat. Mater.*, 2013, **12**, 1050–1056.
- 39 S. Matsuda, M. Ono, S. Yamaguchi and K. Uosaki, Criteria for Evaluating Lithium-Air Batteries in Academia to Correctly Predict their Practical Performance in Industry, *Mater. Horiz.*, 2022, **9**, 856–863.
- 40 W. Chen, W. Yin, Y. Shen, Z. Huang, X. Li, F. Wang, W. Zhang, Z. Deng, Z. Zhang and Y. Huang, High Areal Capacity, Long Cycle Life  $\text{Li-O}_2$  Cathode Based on Highly Elastic Gel Granules, *Nano Energy*, 2018, **47**, 353–360.
- 41 S. Zhao, L. Zhang, G. Zhang, H. Sun, J. Yang and S. Lu, Failure Analysis of Pouch-type  $\text{Li-O}_2$  Batteries with Superior Energy Density, *J. Energy Chem.*, 2020, **45**, 74–82.
- 42 Y. J. Lee, S. H. Park, S. H. Kim, Y. Ko, K. Kang and Y. J. Lee, High-Rate and High-Areal-Capacity Air Cathodes with Enhanced Cycle Life Based on  $\text{RuO}_2/\text{MnO}_2$  Bifunctional Electrocatalysts Supported on CNT for Pragmatic  $\text{Li-O}_2$  Batteries, *ACS Catal.*, 2018, **8**(4), 2923–2934.
- 43 M. Song, H. Tan, X. Li, A. I. Y. Tok, P. Liang, D. Chao and H. J. Fan, Atomic-Layer-Deposited Amorphous  $\text{MoS}_2$  for Durable and Flexible  $\text{Li-O}_2$  Batteries, *Small Methods*, 2020, **4**, 1900274.
- 44 H.-J. Shin, W.-J. Kwak, D. Aurbach and Y.-K. Sun, Large-Scale  $\text{Li-O}_2$  Pouch Type Cells for Practical Evaluation and Applications, *Adv. Funct. Mater.*, 2017, **27**, 1605500.

